Self-assembled 2D supramolecular networks characterized by STM/STS in air and under vacuum

Borislav Naydenov,[†] Samuel Torsney,[†] Alejandro Santana Bonilla,[‡] Mohamed El Garah,[§] Artur Ciesielski,[§] Andrea Gualandi,[||] Luca Mengozzi,[||] Pier Giorgio Cozzi,[||] Rafael Gutierrez,[‡] Paolo Samorì,[§] Gianaurelio Cuniberti,[‡,#,O] and John J. Boland [*,†]

[†]*Centre for Research on Adaptive Nanostructures and Nanodevices (CRANN) & School of Chemistry, Trinity College Dublin, Dublin 2, Ireland,* [‡]*Institute for Materials Sciences and Max Bergmann Center of Biomaterials, TU Dresden, 01062 Dresden, Germany,* [§]*Université de Strasbourg, CNRS, ISIS, 8 alleé Gaspard Monge, 67000 Strasbourg, France,* [||]*ALMA MATER STUDIORUM UNIVERSITÀ DI BOLOGNA, Dipartimento di Chimica "G. Ciamician", Via Selmi 2, 40126 Bologna, Italy,* [#]*Dresden Center for Computational Materials Science (DCCMS), TU Dresden, 01062 Dresden, Germany,* [O]*Center for Advancing Electronics Dresden, TU Dresden, 01062 Dresden, Germany.*

Abstract

We combine ambient (air) and ultra-high vacuum (UHV) scanning tunneling microscopy (STM) and spectroscopy (STS) investigations together with density functional theory (DFT) calculations to gain a sub-nanometer insight into the structure and dynamic of two dimensional (2D) surface-supported molecular networks. The planar tetraferrocene-porphyrin molecules employed in this study undergo spontaneous self-assembly via the formation of hydrogen bonded networks at the gold substrate-solution interface. To mimic liquid phase ambient deposition conditions, film formation was accomplished in UHV by electro-spraying a solution of the molecule in chloroform onto an Au(111) substrate, thereby providing access to the full spectroscopic capabilities of STM that can be hardly attained under ambient conditions. We show that molecular assembly on Au (111) is identical in films prepared under the two different conditions, and in good agreement with the theoretical predictions. However, we observe the contrast found for a given STM bias condition to be different in ambient and UHV conditions despite the similarity of the structures and we propose possible origins of the different imaging contrast. This approach could be valuable for the thorough characterization of surface systems which involve large molecules and are prepared mainly in ambient conditions.

KEYWORDS: air-STM, UHV-STS, DFT, self-assembly, supramolecular networks, tetra-ferrocene-porphyrin.

Introduction

The understanding and control over the use of non-covalent interactions to create complex supramolecular assemblies is of paramount importance in the development of molecular architectures with increasing functional complexity, and is helping to pave the way for disruptive technologies, e.g. in the field of electronics [1] and sensing [2]. While real devices are expected to operate under ambient conditions, it is known that in-depth fundamental studies of the physical properties of molecular architectures at different length scales are best carried out under ultra-high vacuum (UHV). In this regard, the combination of studies in UHV and air environment can offer very important insights into the optimization and the correlation between structure and function in molecular assemblies. A prerequisite of this comparative study is to design experiments where a given molecule undergoes identical self-assembly under the two different environmental conditions [3-5]. The majority of UHV preparation techniques are based on the evaporation/sublimation of components/reagents onto atomically flat and clean surfaces. Scanning tunneling microscopy (STM) is typically the technique of choice to study the process of molecular self-assembly on conducting substrates and combines the highest possible spatial resolution with the possibility of local spectroscopic measurements [6, 7]. In contrast to the UHV environment, in ambient conditions most common preparation involves self-assembly from solution. The fundamental differences between the two assembly approaches can often results in different end products, which has in turn motivated the development of the solid/liquid interface scanning tunneling microscopy (S/L STM) [8, 9] as a first step toward emulating the well-established characterization abilities of the same technique in vacuum (UHV-STM) [10]. Molecular assemblies on conductive substrates can now be studied by STM under different environmental conditions, including UHV, atmospheric pressure imaging of dry films or with the tip immersed into a liquid to investigate the solid/liquid interface, and under electrochemical control. The majority of systems studied by the ambient STM are supramolecular networks which in addition to being investigated as templates for guest molecules [11] can also be functionalized in solution prior to self-assembly leading to one-step deposition of organized monolayers with predesigned properties [12]. Numerous environmental STM imaging studies of supramolecular systems have been reported in the literature [13], yet all still lack the high-quality electronic properties characterization available in UHV scanning tunneling spectroscopy (STS). This deficit is due to the inherent mechanical instability of the approach, bias ranges that are limited by solvent properties, and the inability to perform experiments at the low temperatures required for precise spectroscopic studies. Strategies to overcome these problems rely on *in situ*

electrospray deposition (ESD) [14] or pulse injection deposition [15] of components in solution from ambient to UHV conditions onto clean surfaces and to subsequently characterize the products by UHV-STM. The former method provides better control of the dose and the presence of solvent during deposition provides self-assembly conditions similar to those found in ambient, with the potential to form similar supramolecular assemblies.

The system we consider here comprises of a porphyrin core decorated with ferrocene moieties. Porphyrins have been extensively explored as molecular building blocks for constructing various 2D assemblies because of their unique optoelectronic properties, which make them appealing for numerous applications including photo-catalysis [16, 17] and solar cells [18]. Numerous examples of porphyrin-based architectures on metallic substrates in UHV [19-27] have been reported**.** Noteworthy, under ambient conditions porphyrins substituted with alkyl chains, used in order to increase the energy of physisorption, have been reported to form 2D self-assembled architectures on graphite whose structures have been characterized by STM [22-25, 28-34].

The other component of our system, i.e. Ferrocene (Fc), is an organometallic compound possessing extraordinary optical and electronic properties, which makes it a unique building block for variety of applications in materials science including catalysis [35, 36], sensing [37, 38], and electronics [39]. Thus, control over the self-assembly of ferrocene-containing structures is key towards the exploitation of their optoelectronic characteristics. In particular, ordered Fc-containing structures on a solid surface were recently studied by exploiting hydrogen-bonding between carboxylic acid functionalized Fc's, resulting in the formation of 2D quasicrystals [40]. Recently some of us reported on the self-assembly of guanosine–ferrocene dyads at the graphite/solution interface into free metallic quartet motifs and ribbon architectures. *In situ* STM imaging revealed that ferrocene groups physisorb as a second layer on top of guanosine monolayer structures [41].

The majority of surface systems containing large molecules are prepared and studied mainly in ambient conditions which significantly restricts the availability of high-precision characterization techniques. Here we report the preparation and investigation of molecular networks composed of tetra-phenyl-porphyrin molecules functionalized in their *meso* positions with amide substituents comprising ferrocene electroactive units (see the chemical structures in Figure 1a). These molecular units were assembled into extended 2D networks on Au(111) surfaces so as to yield identical structures under ambient and UHV conditions, and enable a direct comparison of the same network using ambient-STM and UHV-STM. This was possible when using electrospray deposition which ensured that even in vacuum there was sufficient solid-liquid interface during deposition to enable the formation of ordered networks similar to ambient self-assembly. Ambient STM provided detailed insights into the network structure while the cryogenic UHV approach enabled local electronic structure measurements that were

directly compared with the corresponding DFT calculations. We observe excellent agreement between the ambient and the UHV experimental STM results from one side and the theoretical modelling of the molecular network from the other, demonstrating that the electrospray technique is a viable approach to reproduce structures formed by solution processing under ambient conditions.

Experimental section

Sample preparation and measurements under ambient conditions:

M1 and **M2** (see Figure 1) films were prepared by drop casting 100 µL solutions (0.1 mM in $CHCl_3$) onto Au(111); once dried up, the samples were kept in chloroform-saturated atmosphere for 48h at room temperature. The latter solvent vapour annealing (SVA) step in the film preparation was essential to form ordered self-assembled monolayers, by promoting the reorganization of the molecules adsorbed on the surface in the presence of the condensed solvent film. The STM tips were mechanically cut from a Pt/Ir wire (90/10, diameter 0.25 mm). STM measurements were performed using a Veeco scanning tunneling microscope (multimode Nanoscope III, Veeco).

Sample preparation and measurements under UHV*:*

M1 and **M2** islands were prepared *in situ* using commercial electrospray deposition (ESD) source (Molecularspray, UK) attached to an UHV system operating at a base pressure < $1x10^{-10}$ mbar. Applying three-step differential pumping it was possible to deposit solvent and molecules from ambient to 10^{-6} mbar condition on Au(111) substrate kept at room temperature. In our vacuum chamber configuration the measured pressure can differ an order of magnitude from that on the sample thus an effective 10^{-5} mbar is expected on the surface consistent with the presence of a multilayer solvent film during elecrospraying. The latter insured the solid-liquid interface is similar to that in the ambient preparation. The molecules were dissolved in 1:1 Chloroform and Methanol mixture and electrosprayed for 2 min using 1.5 kV and measuring ~10 pA current on the sample. The Au(111) single crystal (Mateck, Germany) was cleaned by cycles of Ar+ sputtering and annealing up to 600K for 3 min.

After preparation the sample was introduced into the UHV-STM (CreaTec, Germany) where it was cooled down to 77K and characterised. dI/dV was measured by lock-in technique applying 10 mV RMS bias modulation.

***DFT calculations*:**

The density-functional theory (DFT) calculations have been carried out using the CP2K [42-49]. Hereby, the GPW formalism has been used in combination with the optimized MOLOPT basis set and completed by an auxiliary plane-wave (PW) expansion used to augment the

electronic charge density for the calculation of the Hartree potential [47, 50]. For the auxiliary basis set a cutoff energy of 550 Ry has been used. For the Hartree-Fock (HF) term an auxiliary density matrix implementation is used as well as an optimized basis set for an accurate HF calculation similar in composition to the polarization consistent (CFIT-3) basis sets derived by Jensen [51]. Based on the ideas of Spencer and Alavi [52] and subsequently developed in CP2K by Guidon *et al.* [53] the PBE0-TC-LR functional has been used throughout this work where the PBE0 hybrid functional has been transformed into a short-range functional without higher computational cost [54, 55]. Van der Waals interactions have been included through the standard D3 semi-empirical approximation that offers a suitable and scalable implementation in order to take into account these forces.

***Synthesis*:**

All reactions were carried under anhydrous conditions using standard Schlenk apparatus. Anhydrous solvents were supplied by Aldrich in Sureseal® bottles and were used as received avoiding further purification. Reagents were purchased from Aldrich or TCI and used without further purification unless otherwise stated. Details are provided in supporting information.

Results and discussion

This work involved the study of two tetraferrocene-porphyrin derivatives designated **M1** and **M2** corresponding to the free base, i.e. the moiety without the metallic centre in the porphyrin core, and its complex with a Zn ion (see Fig. 1a and Experimental section for preparation, synthesis, and characterization). Figure 1 portrays the topographic (STM) images of the **M1** and **M2** self-assembled structures on Au(111) surface recorded under ambient (Fig.1b) and under UHV (Fig. 1c, 1e). In both cases the molecules are found to pack face-on onto the basal plane of the substrate. In ambient conditions the **M1** molecules are resolved in the STM image (see Fig.1b) while the greater imaging resolution achieved in vacuum made it possible to resolve the ferrocene tetramers attached at the edge of each porphyrin (see Fig.1c and 1e). The packing motif monitored are identical for the two cases, with a square unit cell (for which $a = b \sim 2.2$ nm and $\alpha \sim 90^{o}$) and containing a single molecule (see Fig. 1d).

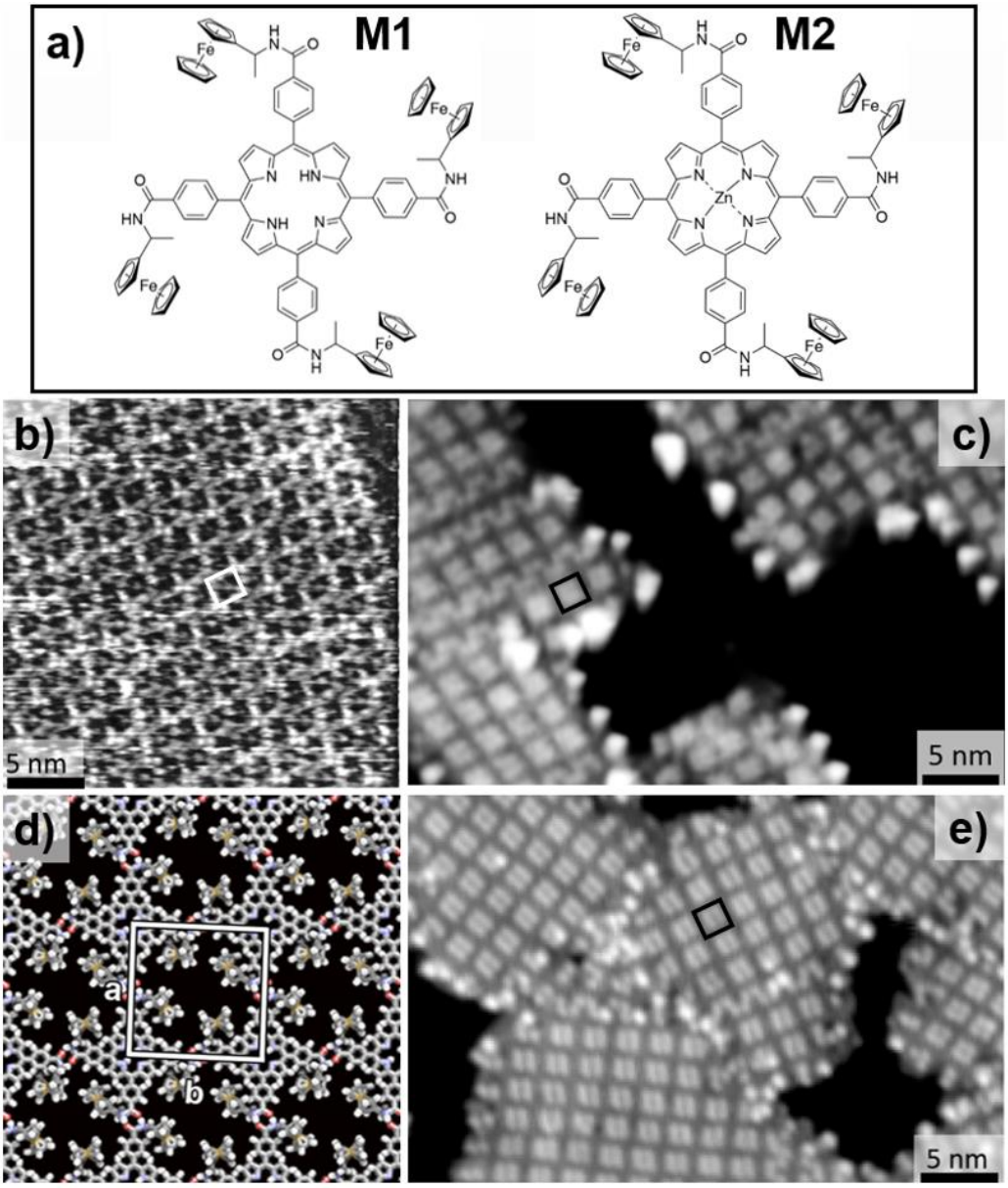

Figure 1. (a) The chemical structures of the two tetraferrocene-porphyrin derivatives (**M1** and **M2**) which self-assembled at solid-liquid interfaces on Au(111) surfaces. (b) STM topographic image of a **M1** film prepared and recorded in air (tunneling current I_t = 25pA and sample bias V_t = +0.55V). 2D molecular networks prepared and studied in UHV are presented with STM topographic images (77K) in (c) for **M1** islands (I_t = 10 pA and V_t = +0.55V) and in (e) for **M2** island (I_t = 10 pA and V_t = +1.0V). (d) The molecular network model which is derived from experiment to be identical for both derivatives with equivalent square unit cell of 2.2x2.2 nm^2 where ferrocenyl quartets are formed. The latter quartets are the dominant features in vacuum STM images in (c) and (e). The unit cell in (d) containing the ferrocenyl quartets are highlighted as squares in (b)-white, (c)-black, and (e)-black. For topographic images with various biases both in air and in vacuum see Fig.3 and supporting information.

Based on the experimentally observed molecular orientation (see Fig.1b, 1c, and 1e), size of the unit cell, and on DFT calculations (see below) we can conclude that the

supramolecular network is stabilized by strong N-H···O hydrogen bonds between secondary amide groups of neighbouring molecules. The DFT modelling also provided insight into the molecule conformation in the normal to the surface direction which is generally poorly resolved in STM. In Figure 2 the total energies of the **M1** and **M2** complexes are plotted versus the molecule-surface distance for the two stable configurations C1 and C2 (depicted on the right hand side of Fig.2). For both derivatives the C1 configuration has the lower adsorption energy (black curves in Fig.2) in which the tetra-phenyl-porphyrin part of the molecule is localized closer to the surface and the ferrocenes pointing away from the surface (see schematics in Fig.2). The molecular core interacts with the surface to immobilize the moiety and the dominant interaction of the porphyrin over the phenyl is probably part of the reasons for the significant difference in the total energy induced by the addition of the zinc.

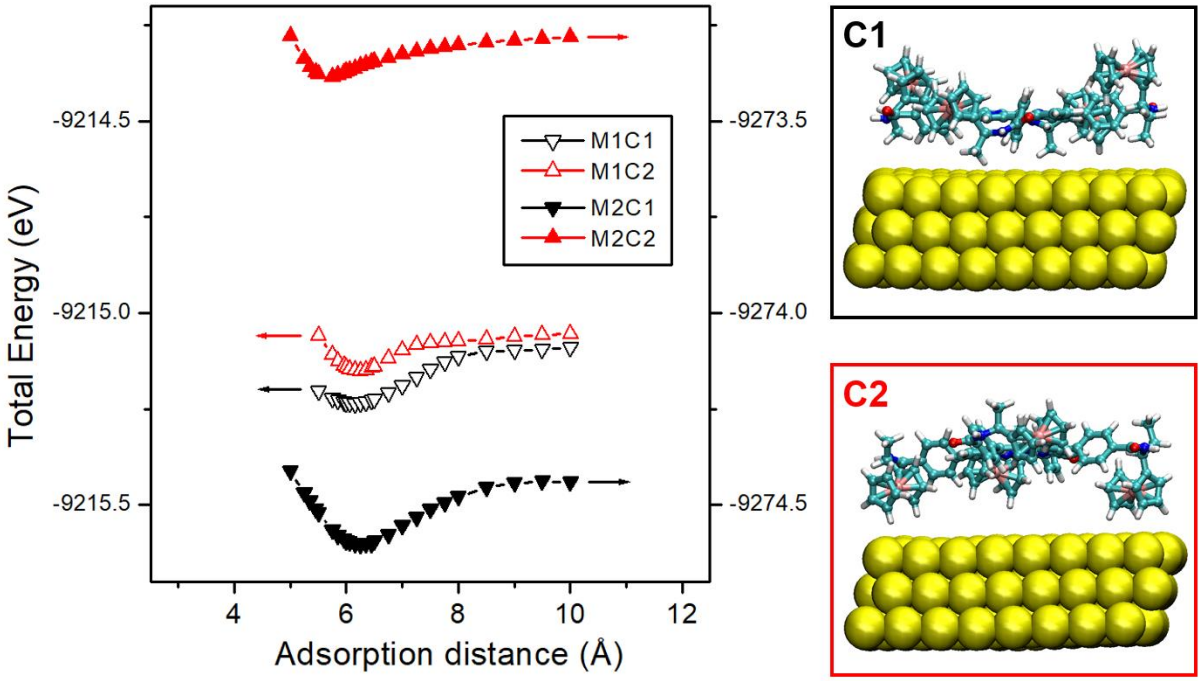

Figure 2. Calculated total energies of the various planar configurations (C1 and C2) of the molecule derivatives **M1** and **M2** on the Au(111) surface in respect to the molecule position normal to the substrate. On the right hand side are presented the side views (C1 and C2) of the optimized unit cells (minima of the total energies) for **M1** which are similar for **M2** (see supporting information).

As was already mentioned the networks demonstrate the same packing in ambient and in vacuum but have different appearance at same tunneling biases (compare Fig.1b and 1c) in the topographic images obtained by air- and by UHV-STM. To track the evolution of the different behaviour in ambient and vacuum tunneling we performed multiple-bias imaging across the entire range from -3V to +3V sample-bias. The results are presented in Figure 3 where UHV-STM (Fig.3a) and air-STM (Fig.3b) are compared. This standard approach to

visualise and identify different parts of the molecule is performed by taking topographic images at various biases so as to include different molecular orbitals in the tunneling-current integral. In the UHV data in Fig.3a protrusions localised on the ferrocenyls dominate all filled-states images (negative sample bias). Note this square quartet pattern is due to four ferrocene moieties from adjacent molecules. This pattern remains qualitatively unchanged even at empty states (positive sample bias) up to +1V. After around +1.5V new topographic features appear and at +3.0V the ferrocenyl related features are no longer distinguishable.

In contrast, ambient STM measurements are restricted to a smaller bias range (±1V) due to instabilities of the tunneling junction. In our air-STM measurements stable images were obtained in the range between -0.6V and +0.6V and the resulting topographic images are presented in Fig.3b. Even in this restricted bias range there are significant variations in the measured topographic images. The ferrocenyl dominated filled-states image at -0.55V is gradually transformed into a tetra-phenyl-porphyrin dominated empty-states image at +0.55V. This qualitative transformation in the air-STM images occurs in the ±1V bias range where in contrast no qualitative image changes were observed in the UHV-STM. This discrepancy between the two characterization approaches appeared despite the identical network-packing at both conditions.

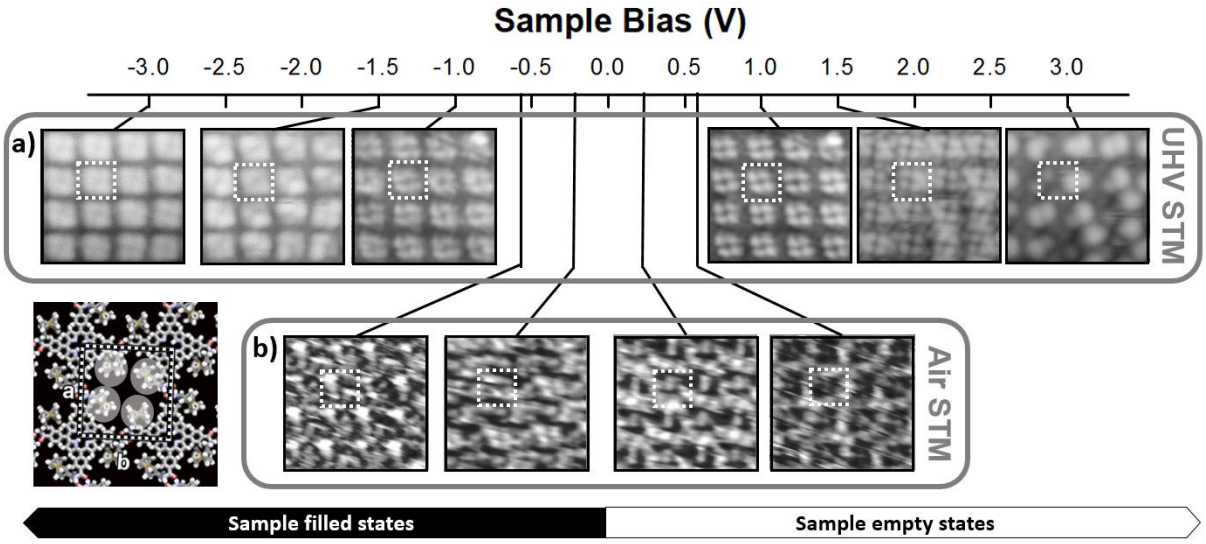

Figure 3. Bias dependant STM-topographic images taken in vacuum (a) and in air (b). All images are connected with their corresponding sample bias on the scale on the figure's top. The insert on the bottom-left shows schematics of the molecular network with highlight of the ferrocenyl quartet which is repeated in all topographic images in (a) and (b) in its position. These results are for **M1** and are identical to those for **M2** (not shown here).

In order to elucidate the origin of the different appearance of the topographic images recorded in air and in vacuum (see Fig.3) and to further characterize the molecular 2D-

assemblies a detailed comparison was undertaken between molecular density of states (DOS) measured by UHV-STM and simulated by theory. In Figure 4a and 4b the evolution of the calculated partial electron density of states (PDOS) is presented by plotting the DOS localized on the various types of atoms of the molecule in gas phase (Fig.4a) and upon adsorption (Fig.4b). The DOS are sums of the projections on the carbon atoms (black curves in Fig.4a, b) and on the iron atoms (red curves in Fig.4a, b). The PDOS of the gas phase is not changed significantly after the adsorption on Au(111) reflecting a relatively weak interaction with the substrate. To quantify this further, we calculated the electron localization function (ELF) for both complexes and obtained values between 0.4 and 0.5 in the space between the molecule and the surface. These values allowed us to conclude that both molecular complexes are physisorbed onto the Au(111) surface (since the ELF value is close to the homogeneous electron gas) and that the main interaction between the Au(111) surface and the molecules is non-covalent in nature.

In Figure 4c the measured local density of states (LDOS) are presented in blue for **M1** and in grey for **M2**. The dI/dV data are measured in a $Z(V)|_I$ mode (feed-back on) and plotted in the bias range below -0.6V and above 0.9V while for the range between these biases the LDOS shown is recovered [56] from dI/dV data measured in an $I(V)|_Z$ mode (feed-back off). The $Z(V)|_I$ mode is typically used for large bias ranges in which the scan does not cross the zero bias where the tip could crash into the surface while attempting to keep the tunneling current constant. In this acquisition mode the signal-to-noise ratio is relatively uniform across all biases. The $I(V)|_Z$ mode where the distance to the surface is controlled is used for bias ranges including the zero bias. In this latter mode the signal-to-noise is not uniform across the bias sweep but could be optimised for particular surface system [56].

The adsorbed molecules have their calculated HOMO-LUMO gap reduced from ~3.2 eV in the gas phase to ~2.7 eV as can be observed in the PDOS data in Fig.4a and 4b. The latter compares well with the experimental value of the HOMO-LUMO gap of ~2.3 eV obtained from the dI/dV spectra of the molecules on Au(111) surface displayed in Figure 4c. The molecular band gap change together with the slight changes in the PDOS peak positions from the gas phase are predominantly due to the structural changes of the molecules upon adsorption. These changes in molecular geometry were studied computationally by varying the planar organic-core gas-phase configurations into a non-coplanar arrangement where ferrocene molecules are tilted and torsionally distorted with respect to the phenyl rings (see schematics in Fig.2). No significant changes in the PDOS spectra were observed due to the presence of the zinc in the **M2** complex, consistent with the absence of any direct interaction between the metal atom and the Au substrate.

In contrast to the STM topographic imaging where the measured parameter is the tunneling current I(V) which is an integral of the LDOS from zero to V, dI/dV imaging provides

a direct visualization of the LDOS amplitude at a specific energy. Thus the experimental dI/dV images at different biases can be directly compared with the theoretical molecule orbitals for various energies. The latter is demonstrated in Figure 4 where the molecular orbital localization images (panels in colour) on the top, above the graphs can be compared with the differential conductance STS images (grey-scale) on the bottom of the figure. Starting from the filled states at biases around -3V, theory shows orbitals predominantly localized on the carbon atoms that extend away from the ferrocene and including the ferrocenyl units themselves. Thus in the corresponding dI/dV image one can clearly resolve the tetra-phenyl-porphyrin core of the molecule. In the -2V to -1V range the PDOS in Figure 4b becomes localised on the iron orbitals within the ferrocenyl units (top -2.0V and -1.25V images in Fig.4) and in the corresponding differential conductance STS images in the same bias range the bright features are localized on the ferrocenyl quartets (see also Fig.1c).

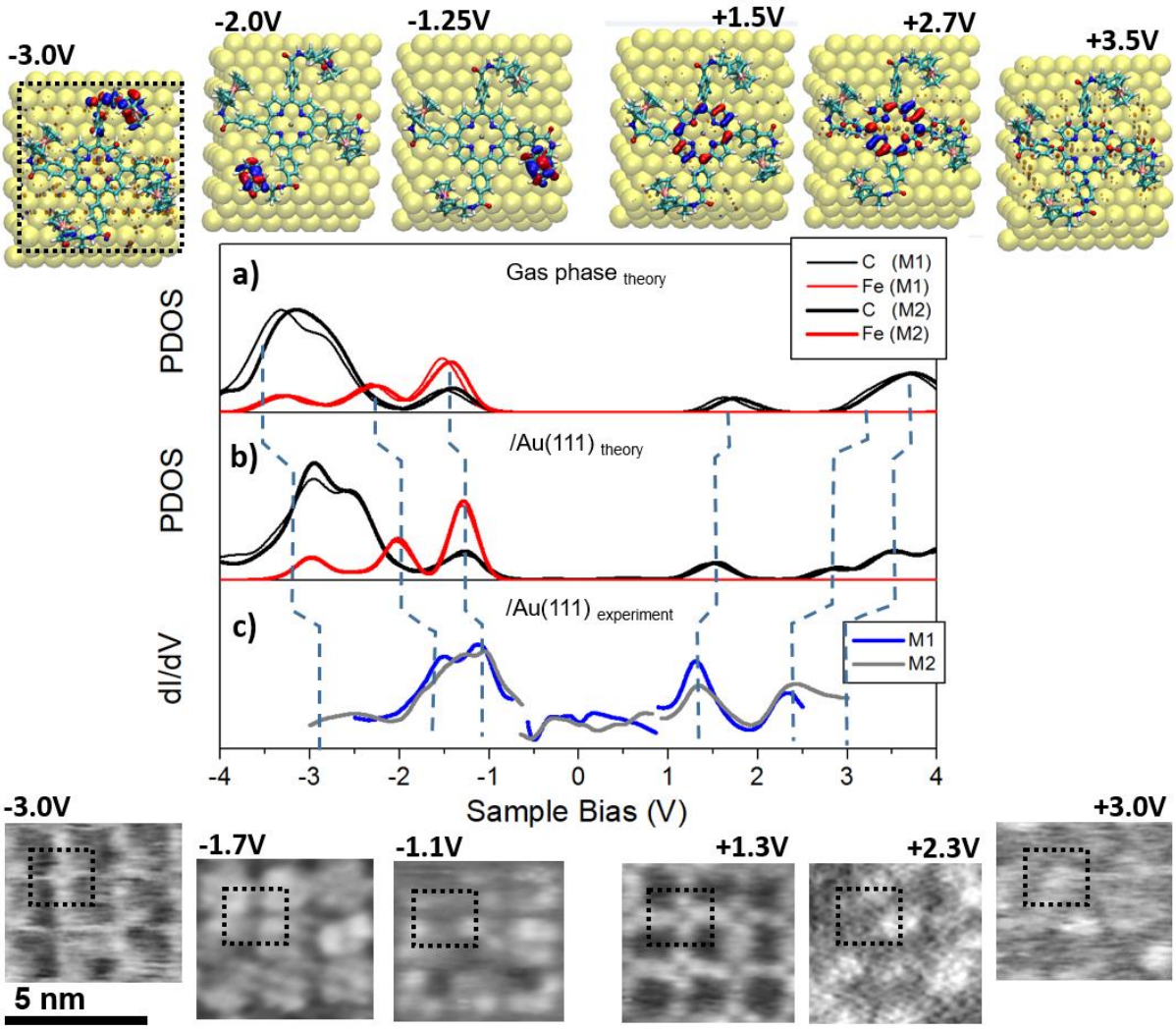

Figure 4. Electron density of states (DOS) projections and spatial localization. The theoretical projected density of states for the molecules in gas phase and upon adsorption on Au(111) surface are plotted in

(a) and (b), respectively. With black curves are shown the projection on the carbon atoms and with red the projections on the iron atoms. The molecular orbitals localization for specific energies are visualized by the pictures on the top. Isosurfaces are plotted with an isovalue of 0.01. Positive regions are in red and negative regions in blue. The experimentally obtained local density of states (LDOS) by UHV-STS are plotted in (c) with blue for the **M1** and grey for the **M2** molecules. The dI/dV spectra in (c) above 0.9V and below -0.6V were recorded in $Z(V)|_{\text{constant I}}$ STS-mode, while the spectra between -0.6V and 0.9V display recovered LDOS [56] from dI/dV spectra recorded in $I(V)|_{\text{predefined Z}}$ STS-mode. On the bottom of the figure are presented experimental dI/dV images (grey scale, white–high, black-low) at the specified sample biases. The vertical dashed lines are representing the evolution of the molecule orbital energy position from (a) through (b) and to (c). The unit cell containing a single molecule is indicated by the dotted square in the top-left corner of each image to help track the evolution of the LDOS projections across the measured bias range.

In the empty states region at positive sample biases in Figure 4b the PDOS is entirely localized on the carbon atoms with the first peak at around 1.5V localized on the porphyrin (see top image in Fig.4). These porphyrin orbitals also dominate the dI/dV image at 1.3V (bottom row in Fig.4). Around 2.5V the carbon localized PDOS spreads from the porphyrin to the phenyl groups of the molecule which can be also detected in the corresponding STS image, the contribution of the non-phenyl carbons is less obvious experimentally. At around 3V all carbon atoms have comparable contribution to the PDOS thus preventing any structural identification of the molecules both in the model and in the experiment.

Based on the results presented in Figure 4 it is possible to determine that the discrepancy between air and vacuum conditions observed in the topographic images shown in Figure 3 are in an energy window associated with HOMO-LUMO gap of the molecular electronic structure. For this reason the molecular DOS cannot play a role in explaining the differences observed in the ±1V bias range in Figure 3 and so we must look to the remaining parameters entering the tunneling current integral; which are the transmission function, the substrate DOS, and the probe DOS. The tunneling transmission function is defined by the work function of the sample which can vary due to a surface dipole induced by the adsorbed molecules. In the theoretical calculations, this interface dipole can be obtained from the change of the work function compared with the pristine metal by the formula: $\Delta\mu = (\varepsilon_0 A/e)\,\Delta\Phi$, where A is the total area of the unit cell, e is the electron charge and ε_0 is the dielectric constant in vacuum. Calculations identified the presence of a surface dipole which lowers the work function by 0.5 eV as shown in Figure 5a. A similar reduction of the work function ($\Delta\Phi$) was observed experimentally when the apparent tunneling barrier-height Φ_A was estimated from *I(Z)* spectra by fitting the $I \sim exp(-\alpha Z \Phi_A^{1/2})$ dependence. Example of such STS data are plotted with circles in Figure 5b together with a topographic image (insert) of the corresponding

surface area where the line profile (grey line) was measured. In Figure 5b one can follow the reduction of the workfunction coming from the bare Au(111) surface onto the **M2** island. In agreement with theory no detectable difference between the **M1** and **M2** complexes was found.

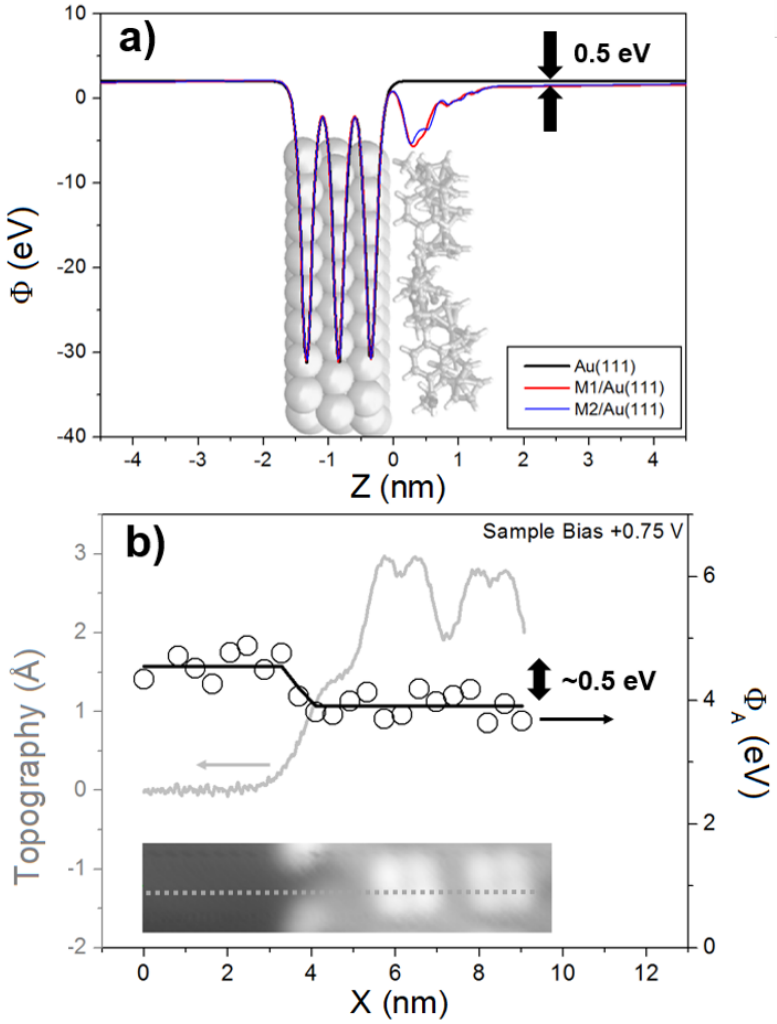

Figure 5. Work function changes upon molecular adsorption. (a) Potentials calculated for bare and after molecule adsorption Au(111) slab. Colour coding is indicated in the same panel. For clarity the side view of the unit cell (see insert C1 in Fig.2) is shown in light grey. Both complexes **M1** and **M2** have their work functions reduced by ~0.5 eV in comparison to the bare gold surface as indicated in the panel (a) with arrows. (b) Apparent barrier height data (circles) obtained by measuring $I(Z)|_{0.75V}$ spectra (feed-back off) along the dotted line on top the inserted in the panel topographic image. The inserted image and the set point for the STS were with 35 pA and 0.75V on a **M2**-island. In panel (b) the measured line profile is plotted with grey.

The significant reduction of the work function (see Fig. 5) over the molecules and thus the increase of the tunneling transmission function can account for the molecular contrast manifested in the topographic images in the HOMO-LUMO gap where the tunneling current-

integral does not explicitly involve the molecular DOS. As the transition function is monotonic as it crosses the zero bias it can qualitatively explain the more-or-less constant contrast in topographic images over the entire ±1V bias range (see Fig. 3a) but cannot account for the polarity dependent changes observed in air (see Fig. 3b). In this bias range only the Au(111) surface state [57] is present and can be observed as weak feature around the zero bias in the LDOS spectra in Figure 4c. Theory predicts the presence of a repulsive interaction (exchange in nature) between the electrons of the closed shell molecular complexes and those from the substrate. Thus, Pauli repulsion due to the rigid molecular electronic cloud pushes the electrons associated with the metal back into the bulk. This effect modulates the metal DOS and can be detected in the energy range around the Fermi level where no molecular features are present and this is an energy range of the Au(111) where the surface state exists. To explore this, planar maps of the calculated gold surface-state were made by integrating the DOS in the -0.5 to 0 range and are presented in Figure 6a. It is clearly seen that the DOS-integral pattern differs significantly between the two molecules **M1** and **M2** reflecting the presence of the zinc ion in **M2**. In general, there is an accumulation of surface state charge density below the porphyrin ring and a reduction next to the ferrocenyl locations. Similar maps were constructed from STS data like those presented in Fig.4c by measuring the intensity of the gold surface state spectra. The latter were then used to construct the schematic maps in Figure 6b from STS spectra exemplified in the LDOS maps in Figure 6c. The LDOS spectra in Figure 6c were recovered [56] from dI/dV measurements taken across the dotted lines in Figures 6a and 6b for the corresponding molecular complex using the $I(V)|_z$ STS mode (feed-back off). Overall there is a good agreement between the theoretical and the experimental patterns of the surface localized density of states due to the molecule adsorption reflecting the presence of the zinc atom in the **M2** complex. Although this subtle modulation in the surface state charge density can be observed experimentally, it is not strong enough to be detected in the topographic images in vacuum or air and thus can be excluded as the source of the difference in the topographic image contrast observed between both (see Fig. 3).

Having eliminated effects due to the molecular DOS, and considered the role of surface dipoles and charge push-back in modulating the transmission function, we are left to conclude that some other factor must be responsible for the different image contrast found under UHV and ambient conditions. This agent must have the capacity to modulate the contrast in air at different bias polarities but must have no effect in vacuum conditions. The presence of a dipole that occurs only in ambient conditions which can change orientation when the polarity of the STM bias is changed could account for the contrast inversion in the images in Figure 3b. It is known [58] that water film are always present on surfaces in air and thus in the tunneling gap of the air-STM. The polar water molecules can easily rotate under the applied strong electric

field and alter the effective surface dipole thus affecting the tunneling barrier height. Additionally the water dipole can perturb significantly the local electric potential and shift the molecular orbital energies below or above the tunneling bias in this way involving or excluding them from the current integral and consequently from the topographic image in ambient conditions**.** In the present case SVA was found to be the only preparation that resulted in the formation of ordered structures on Au(111) surface in ambient conditions. Therefore (without prior thermal annealing) the addition of non-polar solvent for water-free liquid-solid STM would not remove the water molecules from the **M1**/**M2** films as the sample was exposed to air multiple times during preparation.

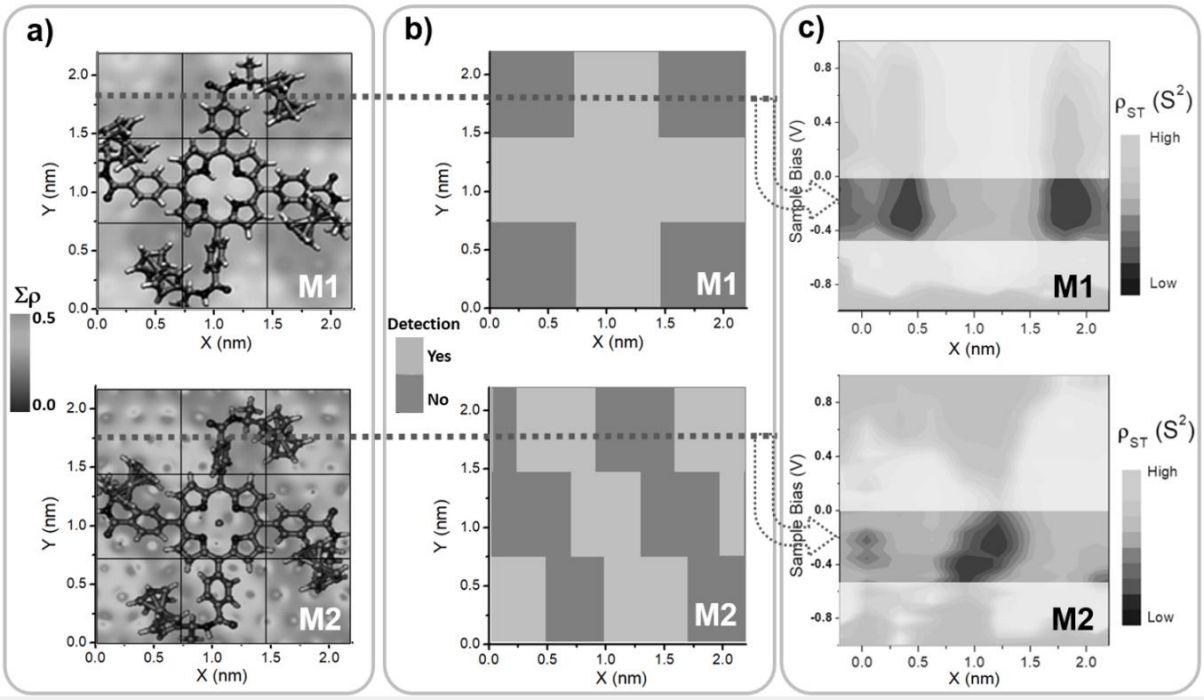

Figure 6. Patterns of the Au(111) surface-localised DOS modulated by the presence of the adsorbed molecules. (a) Theoretical maps of the DOS integral over the -0.5 to 0 eV energy range. (b) Experimental maps of the local detection or non-detection of the metal surface state in the LDOS spectra. (c) Maps of the recovered [56] LDOS from dI/dV measurements taken across the dotted lines in (b) for the corresponding molecular complex in a $I(V)|_Z$ STS mode (feed-back off). In (c) the area of the surface state where the detection was accounted for is highlighted. The position of the molecule is plotted over the maps in (a) and is identical for (b).

Conclusions

In summary, we have visualized with the help of an STM periodic 2D supramolecular networks at the solid/ liquid interface and Au(111) surface. We found that the main interaction between neighbouring molecules consisted on strong N-H···O hydrogen bonds between

secondary amide groups, thereby immobilizing the molecules on the conducting surface. This allowed the characterization of the molecular assemblies with scanning tunneling microscopy (STM) and scanning tunneling spectroscopy (STS) in ambient and in cryogenic UHV environment, respectively. Such STM studies carried out under different environmental conditions revealed identical 2D supramolecules networks. Moreover, no difference in the packing was observed for the two tetraferrocene-porphyrin derivatives one without the metallic centre in the porphyrin core (**M1**), and the other with a Zn ion (**M2**)**.** It was demonstrated that in ambient STM the presence of surface water molecules strongly modulate the local tunneling barrier due to bias dependant dipole re-orientation that shifts the molecular orbitals energy position by the variation in the local electric field.

Finally, we found excellent agreement between the experimental and theoretical density of states (DOS) and work function changes of the adsorbed molecules in the 2D networks. The experimental results presented in this study provided reference solid basis for a comprehensive theoretical study whose predictions in turn added significant information not accessible to the experiment. Thus, more complete description of a system, existing also in ambient conditions, was achieved by air-STM, UHV-STS and DFT calculations. This approach could be valuable for a more complete characterization of surface systems which comprise large molecules and are prepared and studied mainly in ambient conditions.

Associated content

Supporting information

Additional computational details concerning the calculation of the work function, ionization energies and electron affinities using different XC-functionals as well as plots of the Electron Localization function for the two molecular structures studied in this article. Details of molecular synthesis.

Author information

Corresponding Author

*E-mail: jbolnad@tcd.ie

Author contributions

BN, ST, and JB were involved in the UHV STM/STS experiments, analysis, and paper discussions. ASB, RG, and GC were involved in the theoretical modelling and in the paper discussions. MEG, AC, and PS were involved in the ambient STM experiments, analysis, and in the paper discussions. AG, LM, and PGC were involved in the molecular design and synthesis.

Acknowledgements

This work was supported by the European Community through the project EC FP7 ICT-MOLARNET (318516). This work has also been partly supported by the ANR Labex project CSC (ANR-10-LABX-0026 CSC) within the Investissement d'Avenir program ANR-10-IDEX-0002-02, the International Center for Frontier Research in Chemistry (icFRC) and the German Research Foundation (DFG) within the Cluster of Excellence "Center for Advancing Electronics Dresden". Computational resources were provided by the ZIH at Dresden University of Technology.

Abbreviations

STM, scanning tunneling microscopy; STS, scanning tunneling spectroscopy; DFT, density functional theory; UHV, ultra-high vacuum; ESD, electrospray deposition; TPP, tetra-phenyl-porphyrin; CP2K, quantum chemistry and solid state physics software package; GPW, Gaussian and plane wave; MOLOPT, basis set; PW, plane-wave; HF, Hartree-Fock; CFIT-3, basis set; PBE0-TC-LR, hybrid functional; D3, semi-empirical model; ELF, electron localization function; TCI, Tokyo chemical industry; DOS, density of states; LDOS, local density of states; PDOS, partial electron density of states.

References

1. Bassani, D.M., et al., *Harnessing supramolecular interactions in organic solid-state devices: Current status and future potential.* Coordination Chemistry Reviews, 2010. **254**(19-20): p. 2429-2445.
2. Haider, J.M. and Z. Pikramenou, *Photoactive metallocyclodextrins: sophisticated supramolecular arrays for the construction of light activated miniature devices.* Chemical Society Reviews, 2005. **34**(2): p. 120-132.
3. De Marchi, F., et al., *Self-assembly of indole-2-carboxylic acid at graphite and gold surfaces.* Journal of Chemical Physics, 2015. **142**(10).
4. Liu, L., et al., *The Self-Assembled Behavior of DNA Bases on the Interface.* International Journal of Molecular Sciences, 2014. **15**(2): p. 1901-1914.
5. Mazur, U., et al., *Spontaneous solution-phase redox deposition of a dense cobalt(II) phthalocyanine monolayer on gold.* Journal of Physical Chemistry B, 2004. **108**(44): p. 17003-17006.
6. Stipe, B.C., M.A. Rezaei, and W. Ho, *Coupling of vibrational excitation to the rotational motion of a single adsorbed molecule.* Physical Review Letters, 1998. **81**(6): p. 1263-1266.
7. Repp, J., et al., *Molecules on insulating films: Scanning-tunneling microscopy imaging of individual molecular orbitals.* Physical Review Letters, 2005. **94**(2).
8. Sonnenfeld, R. and P.K. Hansma, *Atomic-Resolution Microscopy in Water.* Science, 1986. **232**(4747): p. 211-213.

9. De Feyter, S. and F.C. De Schryver, *Two-dimensional supramolecular self-assembly probed by scanning tunneling microscopy.* Chemical Society Reviews, 2003. **32**(3): p. 139-150.
10. Binnig, G., et al., *Tunneling through a Controllable Vacuum Gap.* Applied Physics Letters, 1982. **40**(2): p. 178-180.
11. Zhang, X.M., Q.D. Zeng, and C. Wang, *Molecular templates and nano-reactors: two-dimensional hydrogen bonded supramolecular networks on solid/liquid interfaces.* Rsc Advances, 2013. **3**(29): p. 11351-11366.
12. Surin, M., et al., *Molecular tectonics on surfaces: Bottom-up fabrication of 1D coordination networks that form 1D and 2D arrays on graphite.* Angewandte Chemie-International Edition, 2007. **46**(1-2): p. 245-249.
13. Ciesielski, A., et al., *Towards Supramolecular Engineering of Functional Nanomaterials: Pre-Programming Multi-Component 2D Self-Assembly at Solid-Liquid Interfaces.* Advanced Materials, 2010. **22**(32): p. 3506-3520.
14. Swarbrick, J.C., J.B. Taylor, and J.N. O'Shea, *Electrospray deposition in vacuum.* Applied Surface Science, 200. **252**.
15. Tanaka, H. and T. Kawai, *Scanning tunneling microscopy imaging and manipulation of DNA oligomer adsorbed on Cu(111) surfaces by a pulse injection method.* Journal of Vacuum Science & Technology B, 1997. **15**(3): p. 602-604.
16. Guo, H.W., et al., *UV-vis spectrophotometric titrations and vibrational spectroscopic characterization of meso-(p-hydroxyphenyl)porphyrins.* Journal of Physical Chemistry B, 2004. **108**(28): p. 10185-10191.
17. Yokoyama, T., et al., *Selective assembly on a surface of supramolecular aggregates with controlled size and shape.* Nature, 2001. **413**(6856): p. 619-621.
18. Yella, A., et al., *Porphyrin-Sensitized Solar Cells with Cobalt (II/III)-Based Redox Electrolyte Exceed 12 Percent Efficiency.* Science, 2011. **334**(6056): p. 629-634.
19. Friesen, B.A., et al., *Differing HOMO and LUMO Mediated Conduction in a Porphyrin Nanorod.* Journal of the American Chemical Society, 2010. **132**(25): p. 8554-+.
20. Pham, T.A., et al., *Heat-induced formation of one-dimensional coordination polymers on Au(111): an STM study.* Chemical Communications, 2015. **51**(77): p. 14473-14476.
21. Spillmann, H., et al., *A two-dimensional porphyrin-based porous network featuring communicating cavities for the templated complexation of fullerenes.* Advanced Materials, 2006. **18**(3): p. 275-+.
22. Auwarter, W., et al., *Self-assembly and conformation of tetrapyridyl-porphyrin molecules on Ag(111).* Journal of Chemical Physics, 2006. **124**(19).
23. Wintjes, N., et al., *A supramolecular multiposition rotary device.* Angewandte Chemie-International Edition, 2007. **46**(22): p. 4089-4092.
24. Ecija, D., et al., *Hierarchic Self-Assembly of Nanoporous Chiral Networks with Conformationally Flexible Porphyrins.* Acs Nano, 2010. **4**(8): p. 4936-4942.
25. Mohnani, S. and D. Bonifazi, *Supramolecular architectures of porphyrins on surfaces: The structural evolution from 1D to 2D to 3D to devices.* Coordination Chemistry Reviews, 2010. **254**(19-20): p. 2342-2362.
26. Marbach, H. and H.P. Steinruck, *Studying the dynamic behaviour of porphyrins as prototype functional molecules by scanning tunnelling microscopy close to room temperature.* Chemical Communications, 2014. **50**(65): p. 9034-9048.
27. Niu, T.C. and A. Li, *Exploring Single Molecules by Scanning Probe Microscopy: Porphyrin and Phthalocyanine.* Journal of Physical Chemistry Letters, 2013. **4**(23): p. 4095-4102.
28. Visser, J., et al., *Two-Dimensional Molecular Patterning by Surface-Enhanced Zn-Porphyrin Coordination.* Langmuir, 2009. **25**(10): p. 5980-5985.

29. Lei, S.B., et al., *STM and XRD studies of the adsorption and assembling structures of phthalocyanine and porphyrin.* Surface and Interface Analysis, 2002. **34**(1): p. 767-771.
30. Wang, H.N., et al., *Chain-length-adjusted assembly of substituted porphyrins on graphite.* Surface and Interface Analysis, 2001. **32**(1): p. 266-270.
31. Otsuki, J., *STM studies on porphyrins.* Coordination Chemistry Reviews, 2010. **254**(19-20): p. 2311-2341.
32. Suto, K., S. Yoshimoto, and K. Itaya, *Electrochemical control of the structure of two-dimensional supramolecular organization consisting of phthalocyanine and porphyrin on a gold single-crystal surface.* Langmuir, 2006. **22**(25): p. 10766-10776.
33. El Garah, M., et al., *Molecular design driving tetraporphyrin self-assembly on graphite: a joint STM, electrochemical and computational study.* Nanoscale, 2016. **8**(28): p. 13678-13686.
34. El Garah, M., et al., *Nanopatterning of Surfaces with Monometallic and Heterobimetallic 1D Coordination Polymers: A Molecular Tectonics Approach at the Solid/Liquid Interface.* Journal of the American Chemical Society, 2015. **137**(26): p. 8450-8459.
35. Diallo, A.K., et al., *"Homeopathic" catalytic activity and atom-leaching mechanism in Miyaura-Suzuki reactions under ambient conditions with precise dendrimer-stabilized Pd nanoparticles.* Angewandte Chemie-International Edition, 2007. **46**(45): p. 8644-8648.
36. Ornelas, C., et al., *Catalytically efficient palladium nanoparticles stabilized by "click" ferrocenyl dendrimers.* Chemical Communications, 2007(46): p. 4946-4948.
37. Astruc, D., M.C. Daniel, and J. Ruiz, *Dendrimers and gold nanoparticles as exo-receptors sensing biologically important anions.* Chemical Communications, 2004(23): p. 2637-2649.
38. Djeda, R., et al., *Click Syntheses of 1,2,3-Triazolylbiferrocenyl Dendrimers and the Selective Roles of the Inner and Outer Ferrocenyl Groups in the Redox Recognition of ATP(2-) and Pd2+.* Angewandte Chemie-International Edition, 2010. **49**(44): p. 8152-8156.
39. Astruc, D., C. Ornelas, and J. Ruiz, *Metallocenyl dendrimers and their applications in molecular electronics, sensing, and catalysis.* Accounts of Chemical Research, 2008. **41**(7): p. 841-856.
40. Wasio, N.A., et al., *Self-assembly of hydrogen-bonded two-dimensional quasicrystals.* Nature, 2014. **507**(7490): p. 86-+.
41. El Garah, M., et al., *Guanosine-based hydrogen-bonded 2D scaffolds: metal-free formation of G-quartet and G-ribbon architectures at the solid/liquid interface.* Chemical Communications, 2015. **51**(58): p. 11677-11680.
42. Frigo, M. and S.G. Johnson, *The design and implementation of FFTW3.* Proceedings of the Ieee, 2005. **93**(2): p. 216-231.
43. Hutter, J., et al., *CP2K: atomistic simulations of condensed matter systems.* Wiley Interdisciplinary Reviews-Computational Molecular Science, 2014. **4**(1): p. 15-25.
44. Krack, M. and M. Parrinello, *All-electron ab-initio molecular dynamics.* Physical Chemistry Chemical Physics, 2000. **2**(10): p. 2105-2112.
45. Lippert, G., J. Hutter, and M. Parrinello, *The Gaussian and augmented-plane-wave density functional method for ab initio molecular dynamics simulations.* Theoretical Chemistry Accounts, 1999. **103**(2): p. 124-140.
46. VandeVondele, J. and J. Hutter, *An efficient orbital transformation method for electronic structure calculations.* Journal of Chemical Physics, 2003. **118**(10): p. 4365-4369.

47. VandeVondele, J. and J. Hutter, *Gaussian basis sets for accurate calculations on molecular systems in gas and condensed phases.* Journal of Chemical Physics, 2007. **127**(11).
48. Krack, M. and M. Parrinelli, *QUICKSTEP: Make the Atoms Dance.* High Performance Computing in Chemistry, 2004. **25**: p. 29-51.
49. VandeVondele, J., et al., *QUICKSTEP: Fast and accurate density functional calculations using a mixed Gaussian and plane waves approach.* Computer Physics Communications, 2005. **167**(2): p. 103-128.
50. Lippert, G., J. Hutter, and M. Parrinello, *A hybrid Gaussian and plane wave density functional scheme.* Molecular Physics, 1997. **92**(3): p. 477-487.
51. Guidon, M., J. Hutter, and J. VandeVondele, *Auxiliary Density Matrix Methods for Hartree-Fock Exchange Calculations.* Journal of Chemical Theory and Computation, 2010. **6**(8): p. 2348-2364.
52. Spencer, J. and A. Alavi, *Efficient calculation of the exact exchange energy in periodic systems using a truncated Coulomb potential.* Physical Review B, 2008. **77**(19).
53. Guidon, M., J. Hutter, and J. VandeVondele, *Robust Periodic Hartree-Fock Exchange for Large-Scale Simulations Using Gaussian Basis Sets.* Journal of Chemical Theory and Computation, 2009. **5**(11): p. 3010-3021.
54. Adamo, C. and V. Barone, *Toward reliable density functional methods without adjustable parameters: The PBE0 model.* Journal of Chemical Physics, 1999. **110**(13): p. 6158-6170.
55. Perdew, J.P., K. Burke, and M. Ernzerhof, *Generalized gradient approximation made simple.* Physical Review Letters, 1996. **77**(18): p. 3865-3868.
56. Naydenov, B. and J.J. Boland, *Variable-height scanning tunneling spectroscopy for local density of states recovery based on the one-dimensional WKB approximation.* Physical Review B, 2010. **82**(24).
57. Schouteden, K., P. Lievens, and C. Van Haesendonck, *Fourier-transform scanning tunneling microscopy investigation of the energy versus wave vector dispersion of electrons at the Au(111) surface.* Physical Review B, 2009. **79**(19).
58. Song, M.B., et al., *Charge transfer through thin layers of water investigated by STM, AFM, and QCM.* Langmuir, 2002. **18**(7): p. 2780-2784.

For Table of Contents Use Only.